14. FLUID DYNAMICS OF THE HEART AND ITS VALVES

Charles S. Peskin and David M. McQueen

14.1 INTRODUCTION

Blood is a viscous incompressible fluid which is propelled through the arteries, capillaries, and veins of the circulation by a collection of elastic and contractile fibers known as the heart. The left side of the heart receives bright red oxygenated blood from the lungs, and it pumps this blood into the aorta through which it is distributed to all of the tissues of the body, including the heart muscle (via the coronary arteries). As it flows through these various tissues, part of the oxygen is removed, and the color changes from bright red to bluish red. At the same time, carbon dioxide that has been generated by tissue metabolism is picked up by the blood. The deoxygenated blood returns to the right side of the heart, which pumps it through the pulmonary arterial tree to the lungs, where the carbon dioxide is removed and the blood becomes once more saturated with oxygen.

Each side of the heart has two chambers, an atrium and a ventricle. Each ventricle has an inflow (atrioventricular) and an outflow (arterial) valve. The valves are primarily passive structures that move in response to the flow of blood, although the atrioventricular valves are supported by muscles that prevent prolapse when those valves are closed. Both types of valves are constructed in such a way that they open freely to allow forward flow but close to prevent backflow. When the ventricles are relaxed (diastole), their inflow valves are open and their outflow valves are closed: during this time period the ventricular pressures are low, and each ventricle fills with blood from the corresponding atrium. When the ventricles contract (systole), the inflow valves close first, and then the outflow valves open as the ventricular pressures rise. Once the outflow valves are open, each ventricle ejects blood into its corresponding artery.

The familiar heart sounds are associated with the closure of the valves and the subsequent vibration of the cardiac and arterial chambers. The lower pitch "Lub" is associated with the nearly synchronous closure of the two atrioventricular valves, and the higher pitched "Dup" is associated with the nearly synchronous closure of the two arterial valves. Valve opening is normally silent but may produce sounds in disease states. Heart murmurs are associated with turbulence that may be generated by jets of fluid that form when valves fail to open fully or fail to close properly.

For further detail concerning the physiology of the heart, see Guy-

ton (1991). The anatomy of the heart will be described in Section 14.6 of the present chapter.

Our concern here is with the mathematical formulation and computer solution of the coupled equations of motion of the blood, the muscular heart walls, and the flexible heart valve leaflets. The goal of the work described herein is to provide a realistic computer model of the heart which can be used in applied studies concerning normal cardiac physiology, diseases affecting the mechanical function of the heart and its valves, and the computer-assisted design of prosthetic cardiac valves. For examples of such studies conducted in an earlier, two-dimensional model of the left heart only, see McQueen et al. (1982); McQueen and Peskin (1983); McQueen and Peskin (1985); Meisner et al. (1985). The present chapter, however, is concerned with a three-dimensional whole-heart model (Peskin and McQueen 1992; Peskin and McQueen 1993; Peskin and McQueen 1995).

14.2 IMMERSED ELASTIC FIBERS IN A VISCOUS INCOMPRESSIBLE FLUID

In this section we formulate the fiber-fluid problem of cardiac dynamics. The formulation that we give involves both fluid dynamics and elasticity theory, coupled together in an unusual way. For background in these two fields, see Chorin and Marsden (1993); Green and Adkins (1970).

Consider an idealized composite material made of elastic fibers embedded in a viscous incompressible fluid. The fibers occupy zero volume fraction, and they have no mass, yet they are so finely divided that a continuum description of the material may be used. The fibers stick to the fluid and move at the local fluid velocity $\mathbf{u}$. At each point of the fiber-fluid composite there is a well-defined fiber direction given by the unit vector $\boldsymbol{\tau}$.

Let (q, r, s) be curvilinear coordinates chosen in such a way that a fixed value of the triple (q, r, s) denotes a material point, and also in such a way that a fixed value of the pair (q, r) designates a fiber. Let

$$\mathbf{x} = \mathbf{X}(q, r, s, t) \tag{14.1}$$

be the position at time t of the material point that carries the label (q, r, s). Then the unit tangent to the fibers is given by

$$\boldsymbol{\tau} = \frac{\partial \mathbf{X}/\partial s}{|\partial \mathbf{X}/\partial s|}. \tag{14.2}$$

Let $T(q, r, s, t)$ be the fiber tension, in the sense that $T\,dq\,dr$ is the force transmitted by the fibers corresponding to the patch $dq\,dr$ of the (q, r) parameter plane. This force points in the fiber direction $\pm\boldsymbol{\tau}$.

Since the fibers are elastic, the fiber tension is related to the fiber strain, which is determined by $|\partial \mathbf{X}/\partial s|$. We use a generalized Hooke's law of the form

$$T = \sigma(|\partial \mathbf{X}/\partial s|; q, r, s, t). \tag{14.3}$$

Note in particular the explicit time dependence of the stress-strain relation (14.3). It is this explicit time dependence that makes it possible for the heart to act as a pump and to do net work on the blood over a cardiac cycle.

We now determine the force applied by the fibers to the fluid in which they are immersed. Consider the collection $\mathcal{S}$ of fiber segments defined by $(q, r) \in \Omega$, $s_1 \le s \le s_2$, where Ω is an arbitrary region of the (q, r) parameter plane, and where s_1 and s_2 (with $s_1 < s_2$) are arbitrary values of the parameter s. Let $\mathcal{F}$ denote the total force applied by the fiber segments in $\mathcal{S}$ to the fluid. Then $-\mathcal{F}$ is the force of the fluid on $\mathcal{S}$. The only other forces acting on $\mathcal{S}$ are the fiber forces transmitted across the surfaces $s = s_1$, and $s = s_2$.

Note that the total force acting on $\mathcal{S}$ must be zero, since the fibers are massless. (As described above, all of the mass is carried by the fluid, which permeates the same space that is occupied by the fibers.) This yields the equation

$$0 = -\mathcal{F} + \int_\Omega (T\boldsymbol{\tau})\, dq\, dr \Big|_{s=s_1}^{s=s_2} \tag{14.4}$$

or, by the fundamental theorem of calculus,

$$\mathcal{F} = \int_{s_1}^{s_2} \int_\Omega \frac{\partial}{\partial s}(T\boldsymbol{\tau})\, dq\, dr\, ds. \tag{14.5}$$

Let

$$\mathbf{f} = \frac{\partial}{\partial s}(T\boldsymbol{\tau}). \tag{14.6}$$

Since s_1, s_2 and Ω are arbitrary, (14.5) shows that $\mathbf{f}$ is the density (with respect to the measure $dqdrds$) of the force applied by the fibers to the fluid in which they are immersed.

For the sake of interpretation, one may expand the derivative in (14.6) to obtain

$$\mathbf{f} = \frac{\partial T}{\partial s}\boldsymbol{\tau} + T\frac{\partial \boldsymbol{\tau}}{\partial s}. \tag{14.7}$$

Note that these two terms are orthogonal: $\boldsymbol{\tau}$ is the unit tangent to the fibers, and $\partial\boldsymbol{\tau}/\partial s$ is the vector whose direction defines the principal normal to the fibers. There is no component of $\mathbf{f}$ in the binormal direction.

In the following, we shall need an expression for the force density in Cartesian coordinates. That is, we require a vector field $\mathbf{F}(\mathbf{x}, t)$ such that

$$\int_V \mathbf{F}(\mathbf{x}, t)\, d\mathbf{x} = \int_{\mathbf{X}^{-1}(V,t)} \mathbf{f}(q, r, s, t)\, dq\, dr\, ds, \tag{14.8}$$

where V is an arbitrary region in the physical space, and where

$$\mathbf{X}^{-1}(V, t) = \{(q, r, s) : \mathbf{X}(q, r, s, t) \in V\} \tag{14.9}$$

This can be achieved by setting

$$\mathbf{F}(\mathbf{x}, t) = \int \mathbf{f}(q, r, s, t)\delta(\mathbf{x} - \mathbf{X}(q, r, s, t))\, dq\, dr\, ds, \tag{14.10}$$

in which the integral extends over the entire (q, r, s) parameter space, and in which $\delta(\mathbf{x})$ is the three-dimensional Dirac delta function. To recover (14.8) from (14.10), integrate over the volume V, interchange the order of integration, and recall that

$$\int_V \delta(\mathbf{x} - \mathbf{X})\, d\mathbf{x} = \begin{cases} 1, \mathbf{X} \in V, \\ 0, \mathbf{X} \notin, V \end{cases} \tag{14.11}$$

Note that $\mathbf{F}(\mathbf{x}, t) = 0$ unless the point $\mathbf{x}$ happens to be within the region that is occupied by the fibers at time t.

Equation (14.10) is not the only way to write the relationship between $\mathbf{F}$ and $\mathbf{f}$. Another possibility, which follows directly from (14.8), is

$$\mathbf{F}(\mathbf{X}(q, r, s, t), t)\, J(q, r, s) = \mathbf{f}(q, r, s, t), \tag{14.12}$$

where

$$J(q, r, s) = \left(\frac{\partial \mathbf{X}}{\partial q} \times \frac{\partial \mathbf{X}}{\partial r} \right) \cdot \frac{\partial \mathbf{X}}{\partial s} \tag{14.13}$$

is the Jacobian of the map $(q, r, s) \to \mathbf{X}(q, r, s, t)$. J is independent of t because the fluid is incompressible. The advantages of using the Dirac delta function as in (14.10) are that it avoids the introduction of J, that it gives an explicit formula for $\mathbf{F}(\mathbf{x}, t)$, and that it generalizes easily to the situation in which the fibers are confined to a (moving) surface embedded in the three-dimensional space, as in the case of a fiber-reinforced heart-valve leaflet. To obtain this generalization, we simply drop one of the two parameters (q or r) that label the fibers. Then the surface in question is given at any particular time t by an equation of the form $\mathbf{x} = \mathbf{X}(r, s, t)$, and we have

$$\mathbf{F}(\mathbf{x}, t) = \int \mathbf{f}(r, s) \delta(\mathbf{x} - \mathbf{X}(r, s, t))\, dr\, ds. \tag{14.14}$$

In this expression there are only two integrals, but the delta function is still three-dimensional, so $\mathbf{F}(\mathbf{x}, t)$ is singular like a one-dimensional delta function. Despite this important difference between the relations given by (14.10), wherein $\mathbf{F}$ is finite, and (14.14), the use of the Dirac delta function provides a unified framework for modeling the thick heart walls and the thin heart-valve leaflets.

14.3 EQUATIONS OF MOTION

Our purpose here is to state the equations of motion of the fiber-fluid system described in the previous section. These equations are as follows

$$\rho \left(\frac{\partial \mathbf{u}}{\partial t} + \mathbf{u} \cdot \nabla \mathbf{u} \right) = -\nabla p + \mu \nabla^2 \mathbf{u} + \mathbf{F}, \tag{14.15}$$

$$\nabla \cdot \mathbf{u} = 0, \tag{14.16}$$

$$\mathbf{F}(\mathbf{x},t) = \int \mathbf{f}(q,r,s,t)\delta(\mathbf{x}-\mathbf{X}(q,r,s,t))\,dq\,dr\,ds, \quad (14.17)$$

$$\frac{\partial \mathbf{X}}{\partial t}(q,r,s,t) = \mathbf{u}(\mathbf{X}(q,r,s,t),t) \quad (14.18)$$

$$= \int \mathbf{u}(\mathbf{x},t)\delta(\mathbf{x}-\mathbf{X}(q,r,s,t))\,d\mathbf{x}, \quad (14.19)$$

$$\mathbf{f} = \frac{\partial}{\partial s}(T\boldsymbol{\tau}), \quad (14.20)$$

$$T = \sigma\left(\left|\frac{\partial \mathbf{X}}{\partial s}\right|; q,r,s,t\right), \quad (14.21)$$

$$\boldsymbol{\tau} = \frac{\partial \mathbf{X}/\partial s}{|\partial \mathbf{X}/\partial s|}. \quad (14.22)$$

Equations (14.15)–(14.16) are the *fluid equations*, (14.20)–(14.22) are the *fiber equations*, and (14.17)–(14.19) are the *interaction equations* of the fiber-fluid system.

Note that the fluid equations are in *Eulerian* form: they involve several unknown functions of $(\mathbf{x},t)$, where $\mathbf{x} = (x_1,x_2,x_3)$ are fixed Cartesian coordinates and t is the time. These unknown functions are the fluid velocity, $\mathbf{u}(\mathbf{x},t)$, the fluid pressure, $p(\mathbf{x},t)$, and the Eulerian fiber force density $\mathbf{F}(\mathbf{x},t)$. The constants ρ and μ are the density and viscosity of the fluid. Equations (14.15)–(14.16) are the familiar Navier-Stokes equations of a viscous, incompressible fluid. The only novel feature is the use of the applied-force density $\mathbf{F}(\mathbf{x},t)$ for the representation of the fiber force.

The fiber equations derived in Section 14.2 are in *Lagrangian* form: they involve several unknown functions of (q,r,s,t), where (q,r,s) are moving curvilinear coordinates attached to the material points of the fibers. These unknown functions are the fiber configuration $\mathbf{X}(q,r,s,t)$, the unit tangent to the fibers $\boldsymbol{\tau}(q,r,s,t)$, the fiber tension $T(q,r,s,t)$ and the Lagrangian form of the fiber force density $\mathbf{f}(q,r,s,t)$. The fiber equations may be used to determine the fiber force density at any given time t from the fiber configuration at that same time t. This is done by substituting (14.21)–(14.22) into (14.20). The fact that the fiber forces can be determined from the fiber configuration is an expression of the elasticity of the fibers.

The interaction equations connect the Lagrangian and Eulerian variables. Note that both of the interaction equations take the form of integral transformations in which the kernel is $\delta(\mathbf{x}-\mathbf{X}(q,r,s,t))$. In (14.17) the integration $(dqdrds)$ is over the fiber parameter space, but in (14.19) the integration $(d\mathbf{x})$ is over the physical space. The latter may be thought of as an integration over the fluid, since the volume fraction occupied by the fibers is zero (see Section 14.2).

The first of the interaction equations (14.17) has already been discussed in Section 14.2. The second interaction equation (14.18)–(14.19) is the no-slip condition of a viscous fluid. In the present context, it states that the fibers move at the local fluid velocity, and it serves as an equation of motion for the fibers, not as a constraint on the fluid motion, since the motion of the fibers is unknown.

The structure of (14.15)–(14.22) is as follows. At any given time t, the state of the system is determined by the fiber configuration $\mathbf{X}(\ ,\ ,\ ,t)$ and the fluid velocity $\mathbf{u}(\ ,t)$. Given these quantities, $\partial\mathbf{X}/\partial t$ may be found directly from (14.18)–(14.19), and $\partial\mathbf{u}/\partial t$ may be determined as follows. First use (14.21) and (14.22) to find T and $\boldsymbol{\tau}$, substitute these results into (14.20) to find $\mathbf{f}$, and then use (14.17) to find $\mathbf{F}$. With $\mathbf{F}$ known, the Navier-Stokes equations, (14.15)–(14.16) may be used to find $\partial\mathbf{u}/\partial t$. (As is well known, this requires the elimination of p through the solution of a Poisson equation.) In effect, then, (14.15)–(14.22) are a first-order system in the state variables $\mathbf{X}$ and $\mathbf{u}$. The numerical solution of this system will be discussed in the following section.

14.4 THE IMMERSED-BOUNDARY METHOD

Equations (14.15)–(14.22) are solved by the immersed-boundary method, see Peskin and McQueen (1992); Peskin and McQueen (1993); Peskin and McQueen (1995), and references therein.

The philosophy underlying the immersed-boundary method is that the fluid equations (14.15)–(14.16), which are in Eulerian form, should be discretized on a fixed cubic lattice, whereas the fiber equations (14.20)–(14.22), which are in Lagrangian form, should be discretized on a moving collection of points that need not coincide with the lattice points of the fluid equations. This immediately raises the question of how to handle the fiber-fluid interaction (14.17)–(14.19), a question which will be answered below through the introduction of a smoothed approximation to the Dirac delta function.

Let time proceed in discrete steps of duration Δt, and use a superscript as the time step index: $\mathbf{X}^n(q,r,s) = \mathbf{X}(q,r,s,n\Delta t)$. Let a discrete collection of fibers be chosen, e.g., $(q,r) = (k\Delta q, \ell\Delta r)$, where k and ℓ are integers, and let each fiber be represented by a discrete collection of points: $s = m\Delta s$, where m is an integer. It is convenient to define the fiber tension and the unit tangent $\boldsymbol{\tau}$ at the "half-integer" points given by $s = (m+\frac{1}{2})\Delta s$.

This is done as follows. For any function $\phi(s)$, let

$$(D_s\phi)(s) = \frac{\phi(s+\frac{\Delta s}{2}) - \phi(s-\frac{\Delta s}{2})}{\Delta s}. \tag{14.23}$$

Then make the definitions

$$T^n = \sigma(|D_s\mathbf{X}^n|; q, r, s, n\Delta t), \tag{14.24}$$

$$\boldsymbol{\tau}^n = \frac{D_s\mathbf{X}^n}{|D_s\mathbf{X}^n|}, \tag{14.25}$$

both of which hold for $s = (m+\frac{1}{2})\Delta s$. Finally, we can use T^n and $\boldsymbol{\tau}^n$ to define $\mathbf{f}^n$ at the points $s = m\Delta s$:

$$\mathbf{f}^n = D_s(T^n\boldsymbol{\tau}^n) \tag{14.26}$$

Note that $\mathbf{f}^n$ is defined at the same values of s as $\mathbf{X}^n$. Equations (14.24)–(14.26) are discrete approximations to (14.21), (14.22), and (14.20), respectively.

Let the fluid velocity and pressure be defined on the cubic lattice of points $\mathbf{x} = \mathbf{j}h$, where h is the meshwidth and $\mathbf{j} = (j_1, j_2, j_3)$ is a vector with integer components. Our next task is to construct a force-field $\mathbf{F}$, defined on this cubic lattice, to represent the effect of the fibers in the fluid-dynamics computation. This done using (14.17) as a guide. The formula for $\mathbf{F}$ is as follows:

$$\mathbf{F}^n(\mathbf{x}) = \sum_{q,r,s} \mathbf{f}^n(q,r,s)\delta_h(\mathbf{x} - \mathbf{X}^n(q,r,s))\Delta q \Delta r \Delta s, \tag{14.27}$$

The notation $\sum_{q,r,s}$ is here understood to mean the sum over the discrete collection of points of the form $(q,r,s) = (k\Delta q, \ell\Delta r, m\Delta s)$, where k, ℓ, m are integers. The function δ_h is a smoothed approximation to the three-dimensional Dirac delta-function. The choice of δ_h will be discussed in the following section.

With $\mathbf{F}^n$ defined, we are ready to solve the Navier-Stokes equations (14.15)–(14.16) on the cubic lattice of meshwidth h introduced above. Note that the Navier-Stokes solver does not need to know anything about the complicated time-dependent geometry of the cardiac fibers, since the influence of those fibers on the fluid is completely described by the forcefield $\mathbf{F}$, which is defined on the regular cubic lattice of the fluid computation. This is the central idea of the immersed-boundary method.

There are many different schemes that could be used to integrate the Navier-Stokes equations. The one that we currently employ is implicitly defined as follows:

$$\rho\left(\tfrac{\mathbf{u}^{n+1}-\mathbf{u}^n}{\Delta t} + \textstyle\sum_{\alpha=1}^3 u_\alpha^n D_\alpha^\pm \mathbf{u}^n\right) - \mathbf{D}^0 p^{n+1}$$
$$= \mu \textstyle\sum_{\alpha=1}^3 D_\alpha^+ D_\alpha^- \mathbf{u}^{n+1} + \mathbf{F}^n, \tag{14.28}$$
$$\mathbf{D}^0 \cdot \mathbf{u}^{n+1} = 0. \tag{14.29}$$

In (14.28)–(14.29), $\mathbf{D}^0$ is the central-difference approximation to ∇, defined by

$$\mathbf{D}^0 = (D_1^0, D_2^0, D_3^0) \tag{14.30}$$

where

$$(D_\alpha^0\phi)(\mathbf{x}) = \frac{\phi(\mathbf{x}+h\mathbf{e}_\alpha) - \phi(\mathbf{x}-h\mathbf{e}_\alpha)}{2h}. \tag{14.31}$$

and where $\{\mathbf{e}_1, \mathbf{e}_2, \mathbf{e}_3\}$ is the standard basis of $\mathbb{R}^3$. Thus $\mathbf{D}^0 p$ approximates ∇p, and $\mathbf{D}^0 \cdot \mathbf{u}$ approximates $\nabla \cdot \mathbf{u}$. The operators $D_\alpha^\pm$ are forward and backward difference approximations to $\partial/\partial x_\alpha$, defined as follows:

$$(D_\alpha^+\phi)(\mathbf{x}) = \frac{\phi(\mathbf{x}+h\mathbf{e}_\alpha) - \phi(\mathbf{x})}{h}, \tag{14.32}$$
$$(D_\alpha^-\phi)(\mathbf{x}) = \frac{\phi(\mathbf{x}) - \phi(\mathbf{x}-h\mathbf{e}_\alpha)}{h}. \tag{14.33}$$

Thus, the expression $\displaystyle\sum_{\alpha=1}^3 D_\alpha^+ D_\alpha^-$, which appears in the viscous term of (14.28), is a difference approximation to the Laplace operator. Similarly, the expression

$\sum_{\alpha=1}^{3} u_\alpha D_\alpha^{\pm}$, which appears in the convection term, is a difference approximation to $\mathbf{u} \cdot \nabla$. In this latter case, the plus or minus sign is chosen to yield upwind differencing:

$$u_\alpha D_\alpha^{\pm} = \begin{cases} u_\alpha D_\alpha^{+}, & u_\alpha < 0, \\ u_\alpha D_\alpha^{-}, & u_\alpha > 0. \end{cases} \tag{14.34}$$

The motivation for this choice of sign can be understood by considering the stability of the difference equation

$$\frac{\phi^{n+1} - \phi^n}{\Delta t} + \sum_{\alpha=1}^{3} u_\alpha^n D_\alpha^{\pm} \phi^n = 0, \tag{14.35}$$

which is a difference approximation to the transport (or advection) equation

$$\frac{\partial \phi}{\partial t} + \mathbf{u} \cdot \nabla \phi = 0. \tag{14.36}$$

With the upwind choice of sign, (14.35) takes the form

$$\phi^{n+1}(\mathbf{x}) = \left(1 - \frac{\Delta t}{h} \sum_{\alpha=1}^{3} |u_\alpha^n(\mathbf{x})|\right) \phi^n(\mathbf{x}) + \frac{\Delta t}{h} \sum_{\alpha=1}^{3} |u_\alpha^n(\mathbf{x})| \phi^n(\mathbf{x} \pm h\mathbf{e}_\alpha). \tag{14.37}$$

Provided that

$$\Delta t \sum_{\alpha=1}^{3} |u_\alpha^n(\mathbf{x})| \le h \tag{14.38}$$

for all $n, \mathbf{x}$, the righthand side of (14.37) is a weighted average. Because of this, we can derive the inequality

$$\max_{\mathbf{x}} |\phi^{n+1}(\mathbf{x})| \le \max_{\mathbf{x}} |\phi^n(\mathbf{x})| \tag{14.39}$$

which says that (14.35) is a *stable* difference scheme. The condition (14.38) is known as the Courant-Friedrichs-Lewy or CFL condition.

It should be mentioned that the upwind difference approximation to $\mathbf{u} \cdot \nabla \mathbf{u}$ used above is only first-order accurate and is just the simplest of a variety of available upwind schemes. For a second-order-accurate upwind scheme, see Bell et al. (1989).

It is important to note that (14.28)–(14.29) provide only an implicit definition of $(\mathbf{u}^{n+1}, p^{n+1})$ given $\mathbf{u}^n$ and $\mathbf{F}^n$. Surprisingly, these equations are linear (with constant coefficients)in the unknowns $\mathbf{u}^{n+1}$ and p^{n+1}; the nonlinear terms of the Navier-Stokes equations are present but have been entirely expressed in terms of $\mathbf{u}^n$. It is therefore natural to use Fourier methods, implemented by the Fast Fourier Transform (FFT) algorithm, to solve for $(\mathbf{u}^{n+1}, p^{n+1})$, see Press et al. (1986).

Since Fourier methods are most easily applied in the context of periodic functions, we choose a periodic cube (3–torus) with period L, as the domain that is occupied by the fluid. The meshwidth h is chosen to be of the form $h = L/N$, where N is an integer, and the computational lattice of points $\mathbf{x_j} = \mathbf{j}h = (j_1 h, j_2 h, j_3 h)$ is chosen to be the set of points given by $j_\alpha \in \{0, 1, \ldots, N-1\}$, for $\alpha = 1, 2, 3$. Arithmetic involving the j_α is understood to be performed modulo N. To accommodate the simplest form of the FFT algorithm, N is chosen to be a power of 2.

Thus, the problem we actually consider is that of a heart immersed in fluid, the fluid being contained in a cubic box with periodic boundary conditions imposed. The fluid external to the model heart may be regarded as representing (in a simplified way) the tissues of the thorax that are adjacent to the heart. These tissues must move when the heart walls move, and they therefore have a (modest) influence on cardiac dynamics. As for the periodic boundary conditions, it should be noted that these are far less restrictive than rigid walls, since they do allow fluid to flow freely through any face of the cube, provided only that such fluid must return instantaneously through the opposite face. Since all points of a 3-torus are equivalent, we do not have to worry about peculiar behavior near the faces of the cube, as we would if rigid-wall boundary conditions had been used. The periodic box does, however, enforce a constant-volume constraint, which is unwanted in the present context, since the volume of the heart changes during the cardiac cycle. This is taken care of through the provision of sources and sinks (including an external source/sink). For ease of exposition, however, we omit the sources and sinks from the present discussion.

The Fourier solution of (14.28) and (14.29) is accomplished as follows. First we rewrite these equations in the form

$$\left(I - \frac{\mu\Delta t}{\rho}\sum_{\alpha=1}^{3} D_\alpha^+ D_\alpha^-\right)\mathbf{u}^{n+1} + \frac{\Delta t}{\rho}\mathbf{D}^0 p^{n+1} = \mathbf{v}^n, \tag{14.40}$$

$$\mathbf{D}^0 \cdot \mathbf{u}^{n+1} = 0, \tag{14.41}$$

where

$$\mathbf{v}^n = \mathbf{u}^n - \frac{\Delta t}{\rho}\sum_{\alpha=1}^{3} u_\alpha^n D_\alpha^{\pm}\mathbf{u}^n + \frac{\Delta t}{\rho}\mathbf{F}^n. \tag{14.42}$$

The three-dimensional discrete Fourier transform is defined as follows. Let $\phi(\mathbf{x})$ be a periodic function with period L in all three space directions. Only the value of ϕ at mesh points will be used in the following definition. Let

$$\begin{aligned}\hat{\phi}(\mathbf{k}) &= \frac{1}{L^3}\sum_{\mathbf{x}} \phi(\mathbf{x}) \exp\left(-i2\pi\frac{\mathbf{k}\cdot\mathbf{x}}{L}\right) h^3 \\ &= \frac{1}{N^3}\sum_{\mathbf{j}} \phi(\mathbf{j}h) \exp\left(-i\frac{2\pi}{N}\mathbf{k}\cdot\mathbf{j}\right).\end{aligned} \tag{14.43}$$

The sums in (14.43) are over the N^3 points given by $j_\alpha \in \{0, 1, \ldots, N-1\}$ for $\alpha = 1, 2, 3$. Here $\mathbf{k} = (k_1, k_2, k_3)$ is a vector with integer components.

Note that $\hat{\phi}(\mathbf{k})$ is periodic in all the components of $\mathbf{k}$ with period N. In the following, we shall restrict k_α to be chosen from the same set as j_α, namely $\{0, 1, \cdots, N-1\}$.

The inversion formula, which is exact at mesh points, is given by

$$\phi(\mathbf{x}) = \sum_{\mathbf{k}} \hat{\phi}(\mathbf{k}) \exp\left(\frac{2\pi i \mathbf{k}\cdot\mathbf{x}}{L}\right) \tag{14.44}$$

or

$$\phi(\mathbf{j}h) = \sum_{\mathbf{k}} \hat{\phi}(\mathbf{k}) \exp\left(\frac{2\pi i}{N}\mathbf{k}\cdot\mathbf{j}\right). \tag{14.45}$$

By considering displacements in $\mathbf{x}$, it is easy to find the Fourier transforms of the difference operators appearing in (14.40)–(14.41). They are

$$\hat{D_\alpha^+}(\mathbf{k})\hat{D_\alpha^-}(\mathbf{k}) = -\frac{4}{h^2}\sin\frac{\pi k_\alpha}{N}, \tag{14.46}$$

$$\hat{\mathbf{D}^0} = \frac{i}{h}\sin\left(\frac{2\pi}{N}\mathbf{k}\right). \tag{14.47}$$

In the latter formula, the expression $\sin(\frac{2\pi}{N}\mathbf{k})$ denotes the vector with components $\sin(\frac{2\pi}{N}k_\alpha), \alpha = 1, 2, 3$. Using these results, we may write the discrete Fourier transformation of (14.40)–(14.41) as follows:

$$A(\mathbf{k})\hat{\mathbf{u}}^{n+1}(\mathbf{k}) + \frac{i\Delta t}{\rho h}\sin\left(\frac{2\pi}{N}\mathbf{k}\right)\hat{p}^{n+1}(\mathbf{k}) = \hat{\mathbf{v}}^n(\mathbf{k}), \tag{14.48}$$

$$\frac{i}{h}\left(\sin\left(\frac{2\pi}{N}\mathbf{k}\right)\right)\cdot\hat{\mathbf{u}}^{n+1}(\mathbf{k}), = 0 \tag{14.49}$$

where

$$A(\mathbf{k}) = 1 + \frac{4\mu\Delta t}{\rho h^2}\sum_{\alpha=1}^{3}\left(\sin\frac{\pi k_\alpha}{N}\right)^2. \tag{14.50}$$

Note that the different values of $\mathbf{k}$ are now uncoupled. This is the (usual) benefit of applying a Fourier transformation to a translation-invariant problem.

For each $\mathbf{k}$, the system (14.48)–(14.49) can be solved for the four unknowns $(\hat{\mathbf{u}}^{n+1}(\mathbf{k}), \hat{p}^{n+1}(\mathbf{k}))$. The solution may be expressed as follows:

$$\hat{\mathbf{u}}^{n+1}(\mathbf{k}) = \frac{\hat{\mathbf{v}}^n(\mathbf{k}) - \frac{i\Delta t}{\rho h}(\sin\frac{2\pi}{N}\mathbf{k})\hat{p}^{n+1}(\mathbf{k})}{A(\mathbf{k})}, \tag{14.51}$$

where

$$\hat{p}^{n+1}(\mathbf{k}) = \frac{\frac{i}{h}(\sin\frac{2\pi}{N}\mathbf{k})\cdot\hat{\mathbf{v}}^n(\mathbf{k})}{-\frac{\Delta t}{\rho h^2}(\sin\frac{2\pi}{N}\mathbf{k})\cdot(\sin\frac{2\pi}{N}\mathbf{k})} \tag{14.52}$$

and where $A(\mathbf{k})$ is given by (14.50)

The values of $\mathbf{k}$ at which $\sin(\frac{2\pi}{N}\mathbf{k}) = (0,0,0)$ require special consideration. There are eight such points in the $\mathbf{k}$-lattice; they are given by $k_\alpha = 0$ or $N/2$, for $\alpha = 1,2,3$. At these special values of the wave vector $\mathbf{k}$,(14.49) is automatically satisfied, and (14.48) reduces to

$$A(\mathbf{k})\hat{\mathbf{u}}^{n+1}(\mathbf{k}) = \hat{\mathbf{v}}^n(\mathbf{k}), \tag{14.53}$$

where $k_\alpha \in \{0, N/2\}$, $\alpha = 1,2,3$. There is no danger of $A(\mathbf{k})$ being zero, since $A(\mathbf{k}) \geq 1$ for all $\mathbf{k}$, see (14.50). Thus, (14.53) determines $\hat{\mathbf{u}}^{n+1}(\mathbf{k})$ at the eight special wave vectors $\mathbf{k}$ that are under consideration here. As for $\hat{p}^{n+1}(\mathbf{k})$, its values at these eight wave vectors are completely arbitrary, so we may set $\hat{p}^{n+1}$ equal to zero at these eight wave vectors in order to have a well-defined pressure.

Once $\mathbf{u}^{n+1}(\mathbf{x})$ has been determined (by applying the inverse FFT algorithm to $\hat{\mathbf{u}}^{n+1}(\mathbf{k})$), the fiber points are moved at the local fluid velocity in this new velocity field. This done according to the following interpolation scheme:

$$\frac{\mathbf{X}^{n+1}(q,r,s) - \mathbf{X}^n(q,r,s)}{\Delta t} = \sum_{\mathbf{x}} \mathbf{u}^{n+1}(\mathbf{x})\delta_h(\mathbf{x} - \mathbf{X}^n(q,r,s))h^3, \tag{14.54}$$

which is a discretization of (14.20). Here $\sum_{\mathbf{x}}$ denotes the sum over the computational lattice $\mathbf{x} = \mathbf{j}h$, $j_\alpha \in \{0, 1, \ldots, N-1\}$, $\alpha = 1,2,3$. Note that the same δ-function weights which are here used for interpolation were previously employed in the application of the fiber force to the computational lattice of the fluid, see (14.27). The construction of the function δ_h will be described in the next section.

In summary, the immersed-boundary method proceeds as follows. Given the fiber configuration $\mathbf{X}^n(q,r,s)$ and the fluid velocity $\mathbf{u}^n(\mathbf{x})$, begin by evaluating the fiber forces $\mathbf{f}^n(q,r,s)$:

$$T^n = \sigma(|D_s\mathbf{X}^n|; q, r, s, n\Delta t), \tag{14.55}$$

$$\boldsymbol{\tau}^n = \frac{D_s\mathbf{X}^n}{|D_s\mathbf{X}^n|}, \tag{14.56}$$

$$\mathbf{f}^n = D_s(T^n\boldsymbol{\tau}^n). \tag{14.57}$$

Next apply the fiber forces to the computational lattice of the fluid:

$$\mathbf{F}^n(\mathbf{x}) = \sum_{q,r,s} \mathbf{f}^n(q,r,s)\delta_h(\mathbf{x} - \mathbf{X}^n(q,r,s))\Delta q\Delta r\Delta s \tag{14.58}$$

Then update the fluid velocity by solving the following system of equations for $(\mathbf{u}^{n+1}, p^{n+1})$:

$$\rho\left(\frac{\mathbf{u}^{n+1} - \mathbf{u}^n}{\Delta t} + \sum_{\alpha=1}^{3} u_\alpha^n D_\alpha^{\pm}\mathbf{u}^n\right) + \mathbf{D}^0 p^{n+1} = \mu\sum_{\alpha=1}^{3} D_\alpha^+ D_\alpha^-\mathbf{u}^{n+1} + \mathbf{F}^n, \tag{14.59}$$

$$\mathbf{D}^0 \cdot \mathbf{u}^{n+1} = 0. \tag{14.60}$$

Finally, interpolate the new velocity field and move the fibers

$$\mathbf{X}^{n+1}(q,r,s) = \mathbf{X}^n(q,r,s) + (\Delta t)\sum_{\mathbf{x}} \mathbf{u}^{n+1}(\mathbf{x})\delta_h(\mathbf{x} - \mathbf{X}^n(q,r,s))h^3 \tag{14.61}$$

Since $\mathbf{X}^{n+1}$ and $\mathbf{u}^{n+1}$ have been found, the time step is complete.

14.5 CONSTRUCTION OF A SMOOTHED δ-FUNCTION

The function $\delta_h(\mathbf{x})$, which plays a prominent role in the immersed-boundary method, is a smoothed approximation to the three-dimensional Dirac δ-function. Let

$$\delta_h(\mathbf{x}) = h^{-3}\phi\left(\frac{x_1}{h}\right)\phi\left(\frac{x_2}{h}\right)\phi\left(\frac{x_3}{h}\right), \tag{14.62}$$

where $\mathbf{x} = (x_1, x_2, x_3)$, and where ϕ has the following properties:

(i) ϕ is a continuous function.

(ii) $\phi(r) = 0$ for $|r| \geq 2$.

(iii) For all r,

$$\sum_{j \text{ even}} \phi(r-j) = \sum_{j \text{ odd}} \phi(r-j) = \frac{1}{2}. \tag{14.63}$$

(iv) For all r,

$$\sum_j (r-j)\phi(r-j) = 0. \tag{14.64}$$

(v) For all r,

$$\sum_j (\phi(r-j))^2 = C, \tag{14.65}$$

where C is independent of r.

We shall show presently that these five postulates uniquely determine the function ϕ, including the specific numerical value of the constant C, and hence (via (14.62)) that they uniquely determine the function δ_h. Before doing so, however, we give an informal discussion of the motivation for proposing these five postulates in the first place.

Continuity of ϕ implies continuity of δ_h, and this avoids sudden changes as the fiber points move in space. An alternative strategy (for example) would be to let each fiber point interact only with the nearest lattice point, but this would introduce spurious discontinuities as the fiber points cross the planes that are equidistant between lattice points.

As a practical matter, bounded support of the function ϕ is essential for the efficient operation of the immersed-boundary method. In the interaction steps, where the function δ_h is used, each fiber point $\mathbf{X}$ interacts with all lattice points $\mathbf{x}$ that lie within the support of $\delta_h(\mathbf{x}-\mathbf{X})$. With the choice $\phi(r) = 0$ for $|r| \geq 2$, each fiber point interacts with exactly $4^3 = 64$ lattice points, already a substantial number. From this standpoint, the support of ϕ should be as small as possible. In postulate (ii), we have made the smallest choice that is consistent with the other postulates.

The third postulate (14.63) immediately implies that, for all r

$$\sum_j \phi(r - j) = 1. \tag{14.66}$$

When δ_h is used for interpolation, this means that the interpolation of constant functions is exact; when it is used for spreading the force to the fluid lattice, this implies conservation of momentum: that the total force is not altered by the spreading process. These considerations do not, however, explain why we need to impose the stronger conditions given by (14.63).

The motivation for these stronger conditions comes from a peculiar property of the central difference operator $\mathbf{D}^0$ that is used in this work as an approximation to the vector differential operator ∇. Of course, $\nabla\phi = 0 \Rightarrow \phi =$constant, but the analogous statement is not true for $\mathbf{D}^0$. As an example, suppose $\phi(\mathbf{j}h) = (-1)^{j_1}$, independent of j_2 and j_3. This function is certainly not constant, it oscillates in the x_1 direction from one lattice point to the next, but $\mathbf{D}^0\phi = 0$ anyway. The effect of this is that spurious long-range oscillations can be introduced into the computed solution by the action of localized forces unless the conditions (14.63) are imposed. These conditions guarantee that the force field $\mathbf{F}$ will have a discrete Fourier transform $\hat{\mathbf{F}}(\mathbf{k})$ that vanishes for any wave vector $\mathbf{k}$ having any component k_α equal to $N/2$.

The fourth postulate, (14.64), when combined with (14.66), guarantees that the interpolation scheme based on δ_h will be exact for any linear function. When δ_h is used for spreading the force to the fluid lattice, these equations guarantee conservation of angular momentum: that the correct total torque is applied to the fluid by each element of the fiber force.

The fifth postulate, (14.65), is motivated an inequality which follows from it by an application of the Schwarz inequality:

$$\sum_j \phi(r_1 - j)\phi(r_2 - j) \leq C \tag{14.67}$$

for all r_1, r_2. Expressions like the one on the lefthand side of this inequality arise when a fiber quantity is applied to the fluid lattice and then interpolated back to the fiber points According to (14.66) and its corollary (14.67), the influence of a fiber point on itself during such an operation is constant, independent of the location of that fiber point with regard to the fluid lattice, and the influence of one fiber point on another is no bigger than the influence of a fiber point on itself.

We now turn to the actual determination of the function ϕ. First note that (14.64) can be simplified through the use of (14.63). The result is

$$\sum_j j\phi(r - j) = r. \tag{14.68}$$

For $r \in [0, 1]$, (14.63), (14.68), and (14.65) read as follows:

$$\phi(r-2) + \phi(r) = \frac{1}{2}, \quad (14.69)$$

$$\phi(r-1) + \phi(r+1) = \frac{1}{2}, \quad (14.70)$$

$$2\phi(r-2) + \phi(r-1) - \phi(r+1) = r, \quad (14.71)$$

$$(\phi(r-2))^2 + (\phi(r-1))^2 + (\phi(r))^2 + (\phi(r+1))^2 = C, \quad (14.72)$$

where we have made use of the postulate that $\phi(r') = 0$ for $|r'| \geq 2$. The constant C can now be determined by setting $r = 0$, and noticing that $\phi(-2) = 0$. With $r = 0$, (14.69) yields $\phi(0) = \frac{1}{2}$, (14.70)–(14.71) imply $\phi(-1) = \phi(1) = \frac{1}{4}$, and (14.72) therefore states that $C = \frac{3}{8}$.

With C known, we can solve for the function ϕ on $[0, 1]$. Equations (14.69)–(14.71) can be used to express $\phi(r-2)$, $\phi(r-1)$, and $\phi(r+1)$ in terms of $\phi(r)$. These results can be substituted with (14.72) to yield a quadratic equation for $\phi(r)$. This equation has two solutions, and it might seem that the choice could be made arbitrarily and separately for each $r \in [0, 1]$, but the postulate of continuity together with the requirement that $\phi(0) = \frac{1}{2}$ (derived above) determines uniquely which solution must be chosen. Once ϕ is known on $[0, 1]$, it can be extended to $[-2, 2]$ by using the abovementioned expressions for $\phi(r-2)$, $\phi(r-1)$, and $\phi(r+1)$ in terms of $\phi(r)$. The result is as follows:

$$\phi(r) = \begin{cases} \dfrac{3 - 2|r| + \sqrt{1 + 4|r| - 4r^2}}{8}, & |r| \leq 1, \\ \dfrac{5 - 2|r| - \sqrt{-7 + 12|r| - 4r^2}}{8}, & 1 \leq |r| \leq 2, \\ 0, & 2 \leq |r|. \end{cases} \quad (14.73)$$

Note that ϕ is an even function, and that not only ϕ but also its derivative is continuous. This last fact is a pleasant surprise, since the continuity of the derivative of ϕ was not one of our postulates.

This completes the construction of ϕ and hence of δ_h. The function ϕ is plotted in Figure 14.1.

14.6 THREE-DIMENSIONAL HEART MODEL

The foregoing sections have described a general numerical method for solving the equations of motion of a viscous incompressible fluid containing an immersed system of elastic or contractile fibers. Our purpose here is to apply that method to the heart. To do so, we must first create an arrangement of fibers in space that mimics the actual layout of muscle fibers in the heart wall and of collagen fibers in the heart-valve leaflets. Elastic parameters, time dependent in the case of the muscle fibers, must also be specified.

We shall not attempt a complete technical description of the heart model here, but the general principles on which it is based will be broadly described. Many of these principles were laid down in the pioneering anatomical

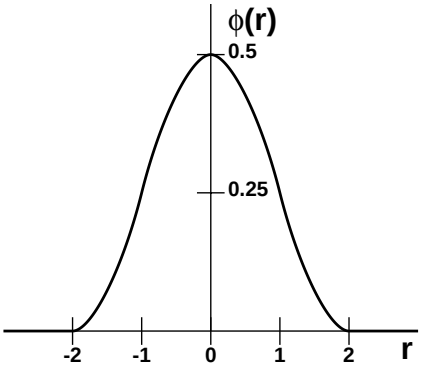

Figure 14.1. One-dimensional delta function.

research of Carolyn Thomas (Thomas 1957), who has given a global qualitative description of the layout of muscle fibers in the left and right ventricles of the mammalian heart. We have also been influenced by Streeter and his colleagues (Streeter, Jr. et al. 1969; Streeter, Jr. et al. 1978) who have made detailed quantitative measurements concerning the distribution of fiber angles in the left ventricular wall.

The two ventricles of the heart together form a somewhat conical structure, with a *base* and an *apex*. In the body, the axis of this cone slopes downward, forward, and leftward as it passes from base to apex. When an anatomical discussion is confined to the heart itself, however, it is customary to think of this axis as though it were vertical, with the base at the top and the apex below. In this viewpoint, which is the one that we shall adopt, the base is a horizontal plane at the top of the venticles. All four valves lie (more or less) within the plane of the base. Above the base one finds the structures to which the ventricles are attached: the left and right atria, the ascending aorta, and the main pulmonary artery.

The conical description of the ventricles that we have given would seem to imply that the ventricles are widest at the base, but this is not quite correct. In fact, there is a plane parallel to the base and slightly below it in which the ventricles achieve their maximum diameter. This is known as the equatorial plane of the heart.

A horizontal cross section of the heart cutting through the left and right ventricles reveals striking asymmetry. The left ventricle is thick walled and roughly circular, whereas the right ventricle is thin walled and crescent shaped. These differences are related to the fact that the pressure developed by the left ventricle is considerably greater (by a factor of about 6) than that of the right ventricle, though the two sides of the heart pump equal volumes of blood per unit time.

According to Thomas (1957), the muscle fibers of the cardiac ventricles begin and end at the valve rings, in the plane of the base of the heart. She describes the fibers as being organized in layers. Each layer has two sheets: one on which the fibers spiral away from the base and another on which they return. The following is a somewhat simplified description of the layers that Thomas found.

Outer/inner layer: The outer sheet of this layer surrounds both ven-

tricles, and the inner sheet forms the innermost lining of the left ventricle. The two sheets meet at the apex of the heart. The fibers of the outer/inner layer have very little swirl. Almost like the rays of a cone, they run nearly directly to the apex along the outer sheet, penetrate the left ventricular wall at the apex (where the wall is very thin), and run almost directly back to the base of the heart along the inner sheet.

Right-inner/left-outer layer: This layer is atypical in that its two sheets lie side by side instead of one inside the other. One sheet forms the inner lining of the right ventricle and the other surrounds the left ventricular wall. The two sheets coincide along the right-ventricular surface of the interventricular septum. On the right-ventricular sheet of this layer, fibers leave the base and spiral clockwise (viewed from above). In the septum, they make a smooth transition to the left-ventricular sheet, after which they spiral counterclockwise (viewed from above) around the left ventricle back to the base of the heart.

Internal left-ventricular layers: These layers make up the bulk of the left-ventricular wall. They are nested, one inside another. As before, each layer has two sheets. Fibers spiral away from the base along the outer sheet, make a smooth transition to the inner sheet where the two sheets meet, and spiral back to the base along the inner sheet.

Although Thomas gives a qualitative discussion of how the fibers run (as summarized above), she does not enunciate a mathematical principle that would determine the fiber paths once the fiber surfaces are known. Such a principle does, however, emerge from the work of Streeter, Jr. et al. (1978), who made detailed measurements of fiber angle in the left ventricular wall.

According to Streeter and his colleagues, the fibers follow geodesic curves on the fiber surfaces. Since the left ventricle has (approximate) axial symmetry, the term "fiber surface" has a well-defined meaning: it is the surface of revolution that one gets by rotating a fiber about the axis of symmetry. Whether the fibers are geodesics on these surfaces or not can be tested by using Clairaut's theorem, that a geodesic on a surface of revolution has $r\cos\phi = \text{constant}$, where r is the radial coordinate (in cylindrical coordinates) and ϕ is the angle between the tangent direction to the geodesic and the circumferential ($\hat{\boldsymbol{\theta}}$) direction. What Streeter and his colleagues actually did was to determine loci of constant $r\cos\phi$, and then to check that these loci were tangent to the fibers. Satisfactory agreement was found, confirming the principle that the fibers are geodesics on the fiber surfaces.

The general method that we use to construct the initial configuration of the model ventricles may now be described. First, we define double-sheeted surfaces on which the fibers lie (see below). In typical cases, the two sheets meet along a common boundary curve somewhere in the interior of the heart wall. The surfaces are generally not tangent where they meet, so the only way that a fiber can make a smooth transition from the sheet to the other is by being locally tangent to the common boundary curve of the two-sheeted surface. This defines an initial direction for each fiber at the common boundary curve, and the fiber can then be continued as a geodesic in both directions along each of the two sheets, until it encounters the valve rings at the base of the heart.

An exception the above description occurs in the case of the right-inner/left-outer layer, where the two sheets of the layer lie side by side and actually share a common surface along the right-ventricular face of the interventricular septum. We think of the transition between the two sheets as be-

ing made at the vertical midline of the common surface, and we assume that the fibers are horizontal there (i.e., perpendicular to the midline). This defines an initial direction, and the fibers can then be contained in both directions as geodesics along the two sheets until they encounter the valve rings at the base of the heart as before.

Below the equator, of the heart, we take all of the surfaces to be portions of cones, although not necessarily cones with circular cross section. In the case of the outer/inner layer and of the right-inner/left-outer layer these conical surfaces extend all the way to the apex of the heart, which is also the common apex of the two cones forming the two sheets of the layer. For the interior layers of the left-ventricular wall, however, we use truncated cones, with the two sheets of the layer meeting along the common curve where this truncation occurs. (This is also the curve along which the fibers make a smooth transition from one sheet to the other.)

All of these conical surfaces must somehow be continued above the equator of the heart, so that they can connect with valve rings in the plane of the base. This process generally involves a bifunction, since a given sheet of a given ventricular layer has a cross section which is a single closed curve in the equatorial plane but which becomes a pair of closed curves in the plane of the valve rings (each ventricle has both an inflow and an outflow valve).

To deal with this situation, we have introduced a fairly general method for constructing a surface whose cross-section in the plane $z = z_1$, consists of n_1 given rings (with nonoverlapping interiors) and whose cross section in the plane $z = z_2$ consists of n_2 given rings (with non-overlapping interiors). By "ring" we just mean a simple closed curve. Note that n_1, and n_2 may be different. If they are, the topology of the cross section necessarily changes as we pass from z_1 to z_2,

Let the n_p rings in the plane $z = z_p$, with $p = 1, 2$, be given in the form $g_{pi}(x, y) = 0, \;\; i = 1 \cdots n_p$, with $g_{pi}(x, y) < 0$ denoting the interior of the ring and with $g_{pi}(x, y) > 0$ denoting its exterior. Since the interiors are nonoverlapping, any point in the plane belongs to at most one of them. It follows that the function

$$G_p(x, y) = \prod_{i=1}^{n_p} g_{pi}(x, y)$$

has the property that $G_p(x, y) < 0$ on the union of the interiors of the various rings in plane p, whereas $G_p(x, y) > 0$ on the intersection of the exteriors in that plane.

Now consider the surface

$$0 = G(x, y, z) = G_1(x, y)\frac{z_2 - z}{z_2 - z_1} + G_2(x, y)\frac{z - z_1}{z_2 - z_1}$$

This has the required cross section in the planes $z = z_1$ and $z = z_2$, and we can hope that it defines a plausible means of interpolating between these cross sections. Unfortunately, this is not guaranteed: sometimes the surface $G(x, y, z) = 0$ has two disconnected components and makes no connection at all between $z = z_1$ and $z = z_2$. We have managed to avoid this possibility in the construction of the heart, and we have therefore been able to use this interpolation scheme to connect the ventricular fiber surfaces to the valve rings.

The surfaces $G(x, y, z) = 0$ do not join smoothly with the conical surfaces that we have constructed below the equator of the heart (the surface normal is discontinuous at the equator), but there is no difficulty continuing a geodesic in a unique way across such an edge, and this lack of smoothness tends to disappear in any case as the heart is pressurized.

The construction that we have just described for determining a surface connecting specified rings in two given planes is also used to build the atria of the model heart. Here, the rings in question are those of the atrioventricular valves and those at which the various veins connect to the atria. Finally the arteries and veins that connect to the heart are initially defined as cylinders with hemispherical caps, on which geodesic fibers are wrapped.

Since the model vessels have blind ends, it is necessary to provide sources and sinks in the hemispherical caps, to simulate the connection of the heart to the rest of the circulation. At present, each such source and sink is connected to a pressure reservoir through a fixed hydraulic resistance. These provide appropriate pressure loads for the model heart. An external source/sink allows for changes in volume as the heart fills and ejects.

The valves of the model heart are also constructed out of fibers. In the case of the atrioventricular valves this is done in much the same style as has been previously described: by defining rather arbitrary initial surfaces and then wrapping fibers as geodesics on these surfaces. For the arterial valves, however, we have found a less arbitrary procedure in which the both the fibers and the surfaces are simultaneously defined by solving a system of partial differential equations. These equations describe the mechanical equilibrium of a one-parameter family of fibers under tension, and their numerical solution determines the closed configuration of the arterial valves (Peskin and McQueen 1994). A future goal is to formulate and solve partial differential equations for the fiber architecture of the heart as a whole. For preliminary results in this direction, see (Peskin 1989).

Finally, we have to consider the elasticity of the model fibers. Let R be the length of a short fiber segment and let T be the tension in that segment. We use a nonlinear length-tension relationship of the form

$$T = \begin{cases} S_0 \left(\dfrac{R - R_0}{R_0} \right)^2, & R \geq R_0, \\ 0, & R \leq R_0, \end{cases}$$

where R_0 is the rest length of the segment and S_0 is a stiffness parameter. Both R_0 and S_0 may be time dependent to simulate active, contractile muscle.

The time dependence R_0 and S_0 can be programmed differently in different parts of the heart, in such a way as to simulate the waves of activation and deactivation that propagate through the cardiac tissue and coordinate the heartbeat. At present, however, we do this only in a rudimentary way: First the atrial muscle contracts synchronously, and then, after a realistic delay, the ventricular muscle contracts synchronously. This procedure ignores the delays that occur within the atria or within the ventricles.

The construction of the model heart is shown in Figures 14.2 through 14.11, and its dynamics are depicted in Figures 14.12 through 14.19.

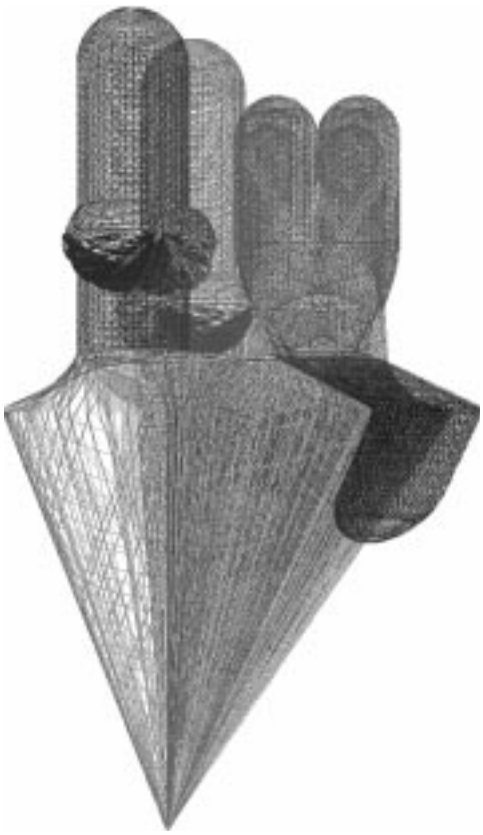

Figure 14.2. Computer model of the heart and the nearby great vessels. The heart is viewed from the front, so the left ventricle is at the lower right, and the thin-walled right ventricle is at the lower left. The vertical vessels at the top of the figure from left to right are the pulmonary artery (in front), the aorta, and two of the four pulmonary veins. The pulmonic and aortic valves (outflow valves of the right and left ventricles, respectively) can be seen within the pulmonary artery and the aorta, and the tricuspid valve (inflow valve of the right ventricle) can just barely be seen at the top of the right ventricle. The mitral valve (inflow valve of the left ventricle) is obscured by the dense left-ventricular wall. The left atrium is visible below the pulmonary veins, and the left-atrial appendage (auricle) is prominently seen hanging over the left-ventricular wall at the right side of the figure. The right atrium is behind the aorta and cannot be seen in this view. The model veins and arteries have blind ends, but sources and sinks are provided, with properties chosen to establish realistic pressure loads on the model heart.

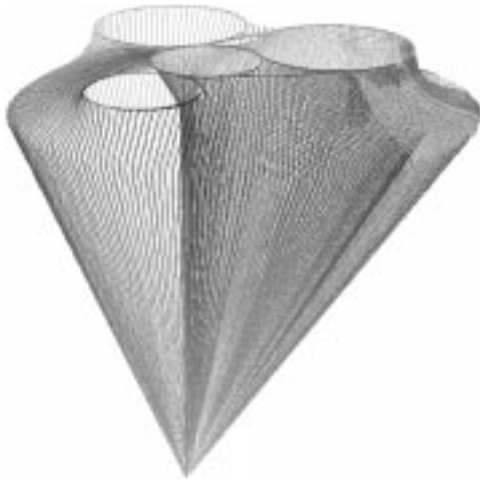

Figure 14.3. The outer/inner layer of the model ventricles. Again, the heart is viewed from the front, so the left ventricle is on the right side of the figure. The four valve rings at the top of the figure form the base of the heart. The larger rings are the locations at which the atria join the ventricles, and the smaller rings are the locations at which the arteries are attached. The fibers of the outer/inner layer form the outermost layer of the ventricles as well as the innermost layer of the left ventricle only.

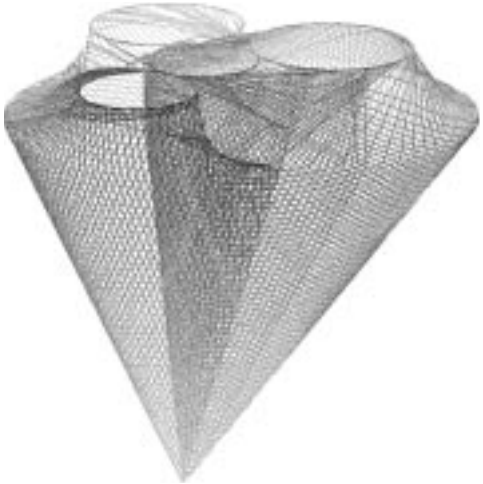

Figure 14.4. The right-inner/left-outer layer of the model ventricles. The fibers of this layer form the inner lining of the right ventricle and the outer lining of the left ventricle. Viewed from the base, these fibers follow a figure-eight trajectory, spiraling clockwise around the right ventricle and then counterclockwise around the left ventricle. The transition is made on the right-ventricular face of the interventricular septum.

Figure 14.5. The internal left-ventricular layers of the model heart are shown in this and the following three figures. The smaller of the two rings at the top of each figure is the aortic-valve ring and the larger is the mitral-valve ring. Each layer is composed of two sheets of fibers which meet at the two valve rings and also at a third ring that forms the lower boundary of that layer. The fibers are tangent to this lower ring and therefore make a smooth transition there from one sheet to the other. The layers are nested, so that both sheets of the smallest layer lie between the two sheets of the next larger layer and so on. Both sheets of the largest of these internal left-ventricular layers lie between the left-ventricular parts of the outer/inner layer and the right-inner/left-outer layer.

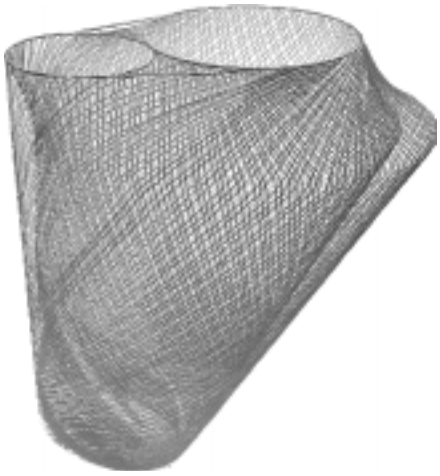

Figure 14.6. An internal left-ventricular layer (see legend of Figure 14.5).

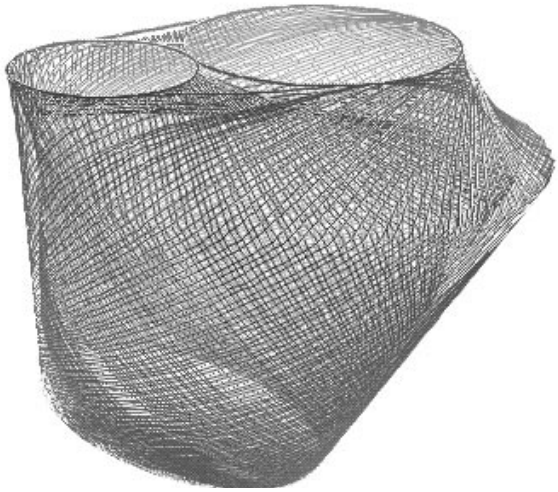

Figure 14.7. An internal left-ventricular layer (see legend of Figure 14.5).

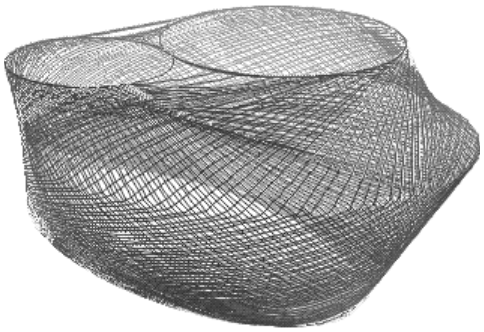

Figure 14.8. An internal left-ventricular layer (see legend of Figure 14.5).

14.7 SUMMARY AND CONCLUSION

This chapter has described the mathematical formulation of the fiber-fluid problem of cardiac mechanics, a technique known as the immersed-boundary method which is suitable for the numerical solution of that problem, and a detailed three-dimensional model of the heart for use in conjunction with the immersed-boundary method.

Both the mathematical formulation and the numerical method described in this chapter are based on the notion that the blood, valves, and muscular heart walls can all be modeled within a common framework. Thus, we think of the cardiac tissues as though they were a part of the fluid, in which, however, there are additional tissue stresses besides those that would normally be present in a fluid. Alternatively, one might say that we think of the blood as a part of the heart, where the stesses that characterize the muscular walls and the elastic heart-valve leaflets happen to be zero.

The computational consequence of this point of view is that we solve the fluid equations on a fixed cubic lattice, unencumbered by the complicated

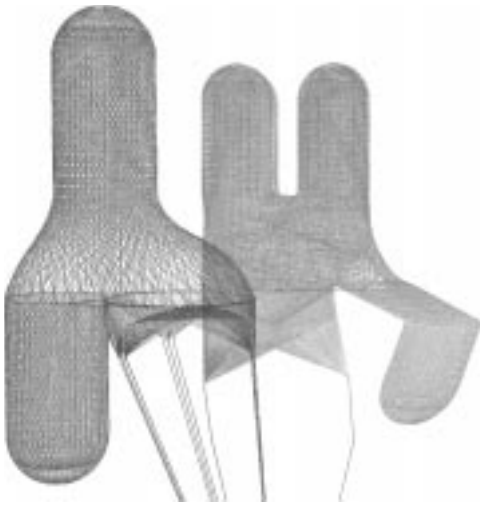

Figure 14.9. Inflow structures of the model heart. At the left side of the figure one sees the superior vena cava (above), the inferior vena cava (below), and the right atrium between them. The right atrium empties through the tricuspid valve, which is seen just to the right of the inferior vena cava. The corresponding structures on the left side of the heart are seen on the right side of the figure. They are the four pulmonary veins, of which two are visible at the top, the left atrium, and the mitral valve. The left-atrial appendage (auricle) is seen at the far right side of the figure.

Figure 14.10. The four valves of the model heart. The outflow (aortic and pulmonic) valves are seen above and the inflow (mitral and tricuspid) valves are seen below. Note that the inflow valves are supported by fans of chordae tendineae, which insert into papillary muscles, two for the mitral and three for the tricuspid valve. The outflow valves, by contrast, are self-supporting.

Figure 14.11. Detail of an outflow (aortic or pulmonic) valve of the model heart.

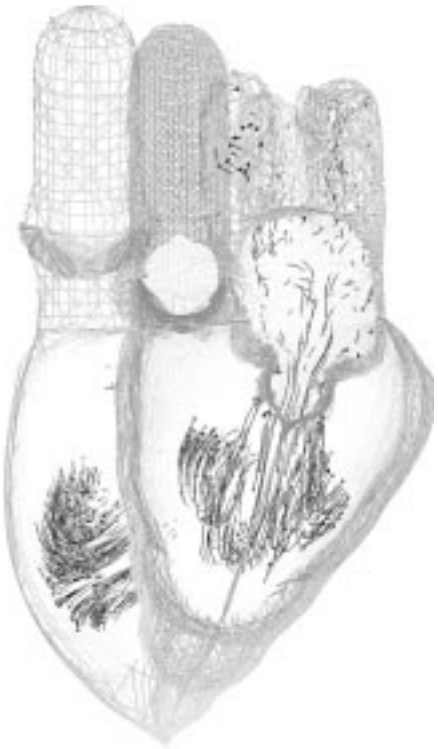

Figure 14.12. Cutaway view of the model heart during early ventricular diastole (relaxation). In this and the figures that follow, the heart model is shown in action. Fluid flow is represented by streaklines, which were computed by tracing the trajectories of particles immersed in the flow. The current position of each such particle is shown as a small blob, and the recent past positions are shown by a fading tail. In this particular figure, only the markers that were initially in the atria are shown. Note the ring vortex visible in the left ventricle (right side of the figure) below the mitral valve.

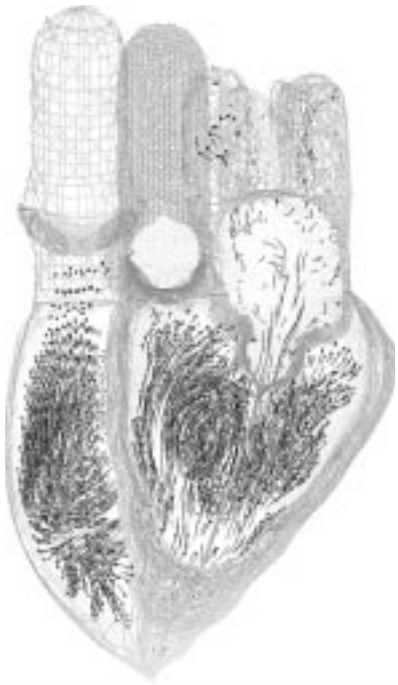

Figure 14.13. Cutaway view of the model heart during early ventricular diastole showing markers that were initially in the ventricles in addition to the atrial markers shown previously in Figure 14.12.

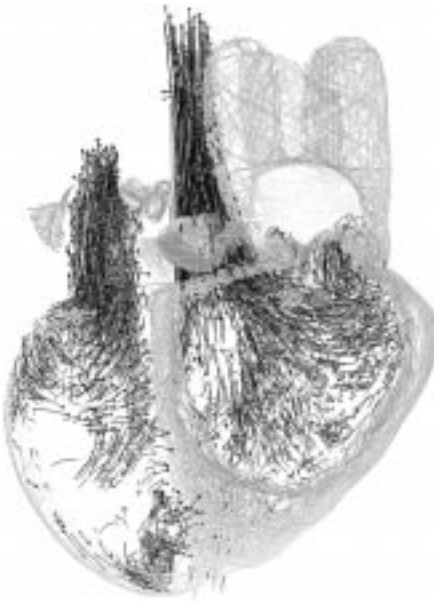

Figure 14.14. Cutaway view of the model heart during ventricular systole (contraction). Only markers that were initially in the ventricles are shown.

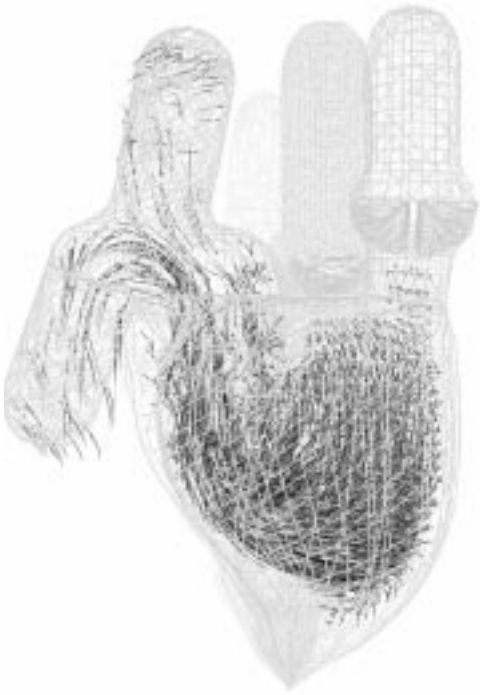

Figure 14.15. Flow pattern in the model right ventricle during early ventricular diastole.

Figure 14.16. Flow pattern in the model right ventricle during late ventricular diastole. Note the prominent vortex that forms in the right ventricle during diastole.

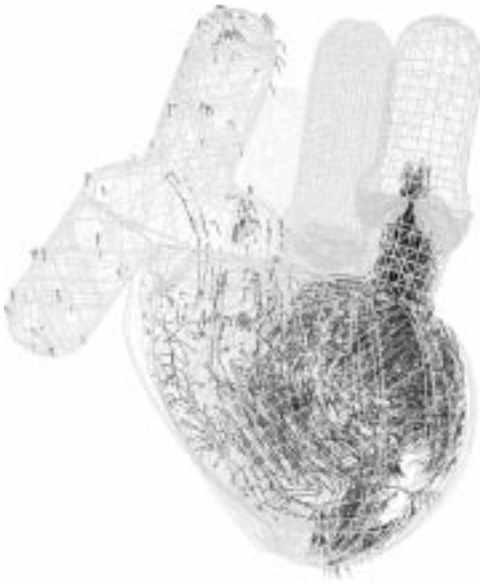

Figure 14.17. Flow pattern in the model right ventricle during ventricular systole.

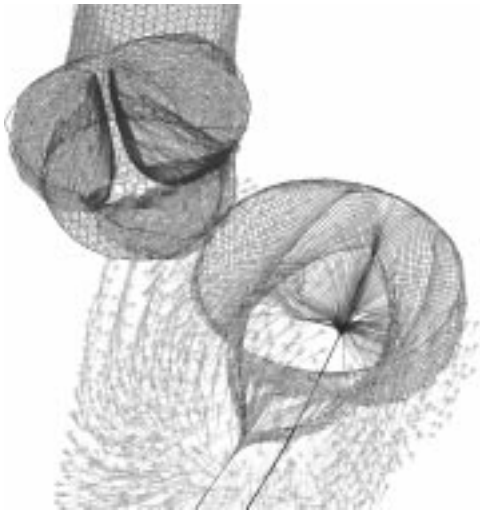

Figure 14.18. Detail of the mitral and aortic valves of the model during ventricular diastole.

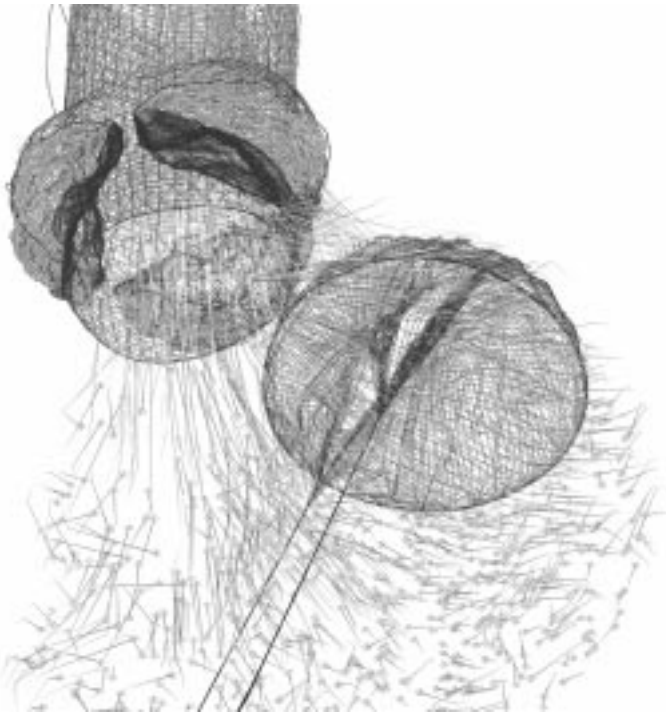

Figure 14.19. Detail of the mitral and aortic valves of the model during ventricular systole.

time-dependent geometry of the heart and its valves. The spatial configuration of those tissues is tracked separately, by means of a collection of tissue marker points that move at the local fluid velocity while simultaneously exerting force on the fluid in which they are immersed. The tissue-fluid interaction is mediated by a smoothed approximation to the Dirac δ-function, which is used both in spreading the fiber forces out onto the computational lattice of the fluid and also in the interpolation of the fluid-velocity field to the marker points of the cardiac tissue fibers.

The computer model that has been created in this way is now ready for use in applied studies concerning the normal and pathological physiology of the heart, and also as a test chamber in the design of prosthetic cardiac valves.

14.8 ACKNOWLEDGMENTS

The work described in this chapter was supported by the National Science Foundation under research grant BIR-9302545. Computation was performed on the Cray C-90 computer at the Pittsburgh Supercomputing Center under a grant (MCA93S004P) from the MetaCenter Allocation Committee. Visualization of results was done at the Academic Computing Facility, New York University. The authors are indebted to Eleen Collins for typesetting the chapter.

REFERENCES

Bell, John B., Colella, Phillip, and Glaz, Harland M. 1989. A second-order projection method for the incompressible Navier-Stokes equations. *Journal of Computational Physics*, **85**(2), 257–283. {*316, 337*}

Chorin, Alexandre J. and Marsden, Jerrold E. 1993. *A Mathematical Introduction to Fluid Mechanics*. New York NY: Springer-Verlag. ISBN 0-387-97918-2. Pages ix + 169. {*310, 337*}

Green, A. E. and Adkins, J. E. 1970. *Large elastic deformations*. Oxford, UK: Clarendon Press. ISBN 0-19-853334-9. Pages xiv + 324. {*310, 337*}

Guyton, Arthur C. 1991. *Textbook of Medical Physiology*. Philadelphia PA: W. B. Saunders Company. ISBN 0-7216-3087-1. Pages 97–109 (of xli + 1014). {*310, 337*}

McQueen, D. M. and Peskin, C. S. 1983. Computer-assisted design of pivoting-disc prosthetic mitral valves. *Journal of thoracic and cardiovascular surgery*, **86**, 126–135. {*310, 337*}

McQueen, D. M. and Peskin, C. S. 1985. Computer-assisted design of butterfly bileaflet valves for the mitral position. *Scandinavian Journal of Thoracic and Cardiovascular Surgery*, **19**, 139–148. {*310, 337*}

McQueen, D. M., Peskin, C. S., and Yellin, E. L. 1982. Fluid dynamics of the mitral valve: physiological aspects of a mathematical model. *American journal of physiology*, **242**, H1095–H1110. {*310, 337*}

Meisner, J. S., McQueen, D. M., Ishida, Y., Vetter, H. O., Bortolotti, U., Strom, J. A., Frater, R. W. M., Peskin, C. S., and Yellin, E. L. 1985. Effects of timing of atrial systole on LV filling and mitral valve closure: computer and dog studies. *American journal of physiology*, **249**, H604–H619. {*310, 337*}

Peskin, C. S. 1989. Fiber-architecture of the left ventricular wall: an asymptotic analysis. *Communications on Pure and Applied Mathematics (New York)*, **42**(1), 79–113. {*326, 337*}

Peskin, C. S. and McQueen, D. M. 1992. Cardiac fluid dynamics. *CRC critical reviews in biomedical engineering*, **20**(5/6), 451–459. {*310, 314, 337*}

Peskin, C. S. and McQueen, D. M. 1993. Computational biofluid dynamics. *Contemporary mathematics*, **141**, 161–186. {*310, 314, 337*}

Peskin, C. S. and McQueen, D. M. 1994. Mechanical equilibrium determines the fractal fiber architecture of the aortic heart valve leaflets. *American journal of physiology*, **266**(1), H319–H328. {*326, 337*}

Peskin, C. S. and McQueen, D. M. 1995. A general method for the computer simulation of biological systems interacting with fluids. *Pages 265–276 of:* Ellington, C. P. and Pedley, T. J. (eds), *Biological Fluid Dynamics: Proceedings of a meeting held at the University of Leeds, UK, 4–8 July 1994*. Symposia of the Society for Experimental Biology, vol. 49. Cambridge, UK: The Company of Biologists Limited. {*310, 314, 337*}

Press, William H., Flannery, Brian P., Teukolsky, Saul A., and Vetterling, William T. 1986. *Numerical Recipes: The Art of Scientific Computing*. Cambridge, UK: Cambridge University Press. ISBN 0-521-30811-9. Pages 390–396; 449–453; and 646–647 (of xx + 818). {*316, 337*}

Streeter, Jr., D. D., Spotnitz, H. M., Patel, D. P., Ross, Jr., J., and Sonnenblick, E. H. 1969. Fiber orientation in the canine left ventricle during diastole and systole. *Circulation research*, **24**, 339–347. {*323, 337*}

Streeter, Jr., D. D., Powers, W. E., Ross, M. A., and Torrent-Guasp, F. 1978. Three-dimensional fiber orientation in the mammalian left ventricular wall. *Pages 73–84 of:* Baan, Jan, Noordergraaf, Abraham, and Raines, Jeff (eds), *Cardiovascular System Dynamics*. Cambridge, MA, USA: MIT Press. {*323, 324, 337*}

Thomas, C. E. 1957. The muscular architecture of the ventricles of hog and dog hearts. *American Journal of Anatomy*, **101**, 17–57. {*323, 337*}